Accepted Manuscript

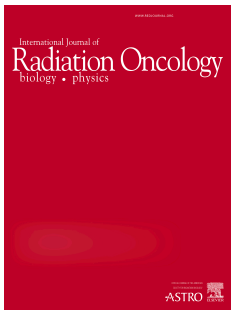

Automatic Segmentation of the Eye in 3D Magnetic Resonance Imaging: A novel Statistical Shape Model for treatment planning of Retinoblastoma

Carlos Ciller, Sandro I. De Zanet, Michael B. Rüegsegger, PhD, Alessia Pica, MD, Raphael Sznitman, PhD, Jean-Philippe Thiran, PhD, Philippe Maeder, MD, Francis L. Munier, MD, Jens H. Kowal, PhD, Meritxell Bach Cuadra, PhD

PII: S0360-3016(15)00299-0

DOI: 10.1016/j.ijrobp.2015.02.056

Reference: ROB 22816

To appear in: *International Journal of Radiation Oncology • Biology • Physics*

Received Date: 16 September 2014

Revised Date: 18 February 2015

Accepted Date: 25 February 2015

Please cite this article as: Ciller C, De Zanet SI, Rüegsegger MB, Pica A, Sznitman R, Thiran J-P, Maeder P, Munier FL, Kowal JH, Cuadra MB, Automatic Segmentation of the Eye in 3D Magnetic Resonance Imaging: A novel Statistical Shape Model for treatment planning of Retinoblastoma, *International Journal of Radiation Oncology • Biology • Physics* (2015), doi: 10.1016/j.ijrobp.2015.02.056.

Title:
Automatic Segmentation of the Eye in 3D Magnetic Resonance Imaging: A novel Statistical Shape Model for treatment planning of Retinoblastoma

Authors:
Carlos Ciller[1,2,6];
Sandro I. De Zanet[2,7];
Michael B. Rüegsegger[2,7], PhD;
Alessia, Pica[3], MD ;
Raphael Sznitman[2,7], PhD;
Jean-Philippe Thiran[4,1], PhD;
Philippe Maeder[1], MD ;
Francis L. Munier[5], MD ;
Jens H. Kowal[2,7], PhD ;
Meritxell Bach Cuadra[6,1,4], PhD;

1. Department of Radiology, Lausanne University Hospital (CHUV) and University of Lausanne (UNIL), Lausanne, Switzerland
2. Ophthalmic Technology Group, ARTORG Center of University of Bern, Bern, Switzerland
3. Department of Radiation Oncology, Inselspital, Bern University Hospital, Bern, Switzerland
4. Signal Processing Laboratoy (LTS5), École Polytechnique Fédérale de Lausanne (EPFL), Lausanne, Switzerland
5. Unit of Pediatric Ocular Oncology, Jules Gonin Eye Hospital, Lausanne, Switzerland
6. Centre d'Imagerie BioMédicale (CIBM), University of Lausanne (UNIL), Lausanne, Switzerland
7. Department of Ophthalmology, Inselspital, Bern University Hospital, Bern, Switzerland

Corresponding author:
Carlos Ciller
PhD Candidate at CIBM

Medical Image Analysis Laboratory (MIAL) - http://www.unil.ch/mial/
Department of Radiology,
Centre Hospitalier Universitaire Vaudois (CHUV) and University of Lausanne (UNIL)
Rue du Bugnon 46, CH-1011 Lausanne, Switzerland
Email: carlos.cillerruiz@unil.ch
Phone: (+41) 21 314 75 31

Universität Bern
ARTORG Center for Biomedical Engineering Research
Ophthalmic Technologies Laboratory,
Murtenstrasse 50
CH-3010 Bern
Email: carlos.ciller@artorg.unibe.ch

Shortened running title: (<40 characters):
Automatic Segmentation of the Eye in 3D MRI

Acknowledgment:
This work is supported by a grant from the Swiss Cancer League (KFS-2937-02-2012). This work is also supported by the Centre d'Imagerie BioMédicale (CIBM) of the University of Lausanne (UNIL), the École Polytechnique Fédérale de Lausanne (EPFL), the University of Geneva (UniGe), the Centre Hospitalier Universitaire Vaudois (CHUV), the Hôpitaux Universitaires de Genève (HUG), the University of Bern (UniBe) and the Leenaards and the Jeantet Foundations.

Conflict of Interest Notification:

Mr. Ciller has nothing to disclose. Mr. De Zanet has nothing to disclose. Dr. Rüegsegger has nothing to disclose. Dr. Pica has nothing to disclose. Dr. Sznitman has nothing to disclose. Dr. Thiran has nothing to disclose. Dr. Maeder has nothing to disclose. Dr. Munier has nothing to disclose. Dr. Kowal has nothing to disclose. Dr. Bach Cuadra has nothing to disclose.

Title:

Automatic Segmentation of the Eye in 3D Magnetic Resonance Imaging: A novel Statistical Shape Model for treatment planning of Retinoblastoma

Summary:

The diagnosis and treatment of retinoblastoma requires often the laborious task of segmenting the eye anatomy in 3D magnetic resonance images (MRI). Statistical Shape Modeling (SSM) techniques are successful tools for modeling anatomical shapes in medical imaging. This work introduces the first fully automatic segmentation of the eye evaluated on 24 MRI children eyes, yielding overlap measures of 94.90±2.12% for the sclera and cornea, 94.72±1.89% for the vitreous humor and 85.16±4.91% for the lens.

Abstract:

Purpose: Proper delineation of ocular anatomy in 3D imaging is a big challenge, particularly when developing treatment plans for ocular diseases. Magnetic Resonance Imaging (MRI) is nowadays utilized in clinical practice for the diagnosis confirmation and treatment planning of retinoblastoma in infants, where it serves as a source of information, complementary to the Fundus or Ultrasound imaging. Here we present a framework to fully automatically segment the eye anatomy in the MRI based on 3D Active Shape Models (ASM), we validate the results and present a proof of concept to automatically segment pathological eyes.

Material and Methods: Manual and automatic segmentation were performed on 24 images of healthy children eyes (3.29±2.15 years). Imaging was performed using a 3T MRI scanner. The ASM comprises the lens, the vitreous humor, the sclera and the cornea. The model was fitted by first automatically detecting the position of the eye center, the lens and the optic nerve, then aligning the model and fitting it to the patient. We validated our segmentation method using a leave-one-out cross validation. The segmentation results were evaluated by measuring the overlap using the Dice Similarity Coefficient (DSC) and the mean distance error.

Results: We obtained a DSC of 94.90±2.12% for the sclera and the cornea, 94.72±1.89% for the vitreous humor and 85.16±4.91% for the lens. The mean distance error was 0.26±0.09mm. The entire process took 14s on average per eye.

Conclusion: We provide a reliable and accurate tool that enables clinicians to automatically segment the sclera, the cornea, the vitreous humor and the lens using MRI. We additionally present a proof of concept for fully automatically segmenting pathological eyes. This tool reduces the time needed for eye shape delineation and thus can help clinicians when planning eye treatment and confirming the extent of the tumor.

Introduction

Retinoblastoma is the most common intraocular tumor in children and affects roughly one in every 18.000 newborns worldwide[1,2]. With 90% of cases identified by the age of three, most retinoblastomas are curable, especially when the tumor is confined to the area between the retina and the surface of the vitreous humor (VH)[3]. For this reason, accurate and non-invasive techniques that can be used for early diagnosis assessment and the tumor extent follow-up or treatment planning are critical.

Today, Fundus image photography and 2D Ultrasound (US) are the key image modalities of choice for the diagnosis and follow-up of intraocular tumors[4]. Computed Tomography (CT) is often regarded as a superior tool for the detection of intra-tumoral calcifications within the eye cavity, however, it induces ionizing radiation, which has a more negative effect on children than adults. Furthermore, ionizing radiation has been shown to modify the patient's radio-susceptibility (RS), thus affecting the carriers of the RB1 germline mutation that are responsible for retinoblastoma. Moreover, there is very little evidence regarding the diagnostic accuracy of CT in the context of advanced retinoblastoma[5] and thus, it is less recommended for imaging the disease[3].

Over the last decade, the ophthalmic community has become increasingly interested in Magnetic Resonance Imaging (MRI)[6], mainly due to the favorable tissue contrast and improved image resolution[7]. MRI sequences provide a remarkable soft tissue information source, with the resolution comparable to the information extracted from CT[8]. Additionally, recent studies[3,9] have provided direct evidence for the usefulness of MRI in both diagnosis and the treatment follow-up of retinoblastoma, and that the combination of both MRI and US would be sufficient to account for all calcifications found using CT. Consequently, quantitative analysis of the eye MR images is needed to support the diagnosis and therapy planning with a better and faster eye anatomy delineation. In this context, the existence of a robust and accurate segmentation tool for eye MR images would offer an unprecedented opportunity for multimodal patient specific eye modeling. That is, combining modalities such as Fundus imaging, US with MRI for treatment planning of the eye[10–12].

Until now, the task of segmenting the eye in medical imaging has been completed predominantly by using a pre-established sets of parameters. EYEPLAN[13], a framework that estimated the shape of the lens, the cornea and the sclera, does so by combining parametric spheres. In comparison, OCTOPUS[14], currently widely used in modeling the eye inside CT, employs the same concept but models the eye as combinations of ellipsoids. Both these methods require an expert to pre-select visual landmarks. In addition, they have constrained modeling capabilities, as they limit the eye-growing pattern as a linear function dependent on the age of the patients. As such, they do not accommodate for a free growing pattern that is representative of a real eye population. The recent image processing techniques have opened the door to designing more complex models, which enable the segmentation of more regions of interest (ROI) within the eye. In 2006, Singh et al.[15] proposed a segmentation method for MRI based on spherical meshes that leveraged the posterior corneal pole and an sphericity modifying parameter. More recently, Bach Cuadra et al.[8] designed an algorithm combining parametric active contours with an ellipsoid model, which offered more accurate segmentations of the sclera and the lens on the CT and US images. Despite these advances, the eye treatment planning is far from being optimal.

One key element lacking in the above parametric models is the statistical information that can be extracted from the variability of a population. This type of information is offered by Statistical Shape Models (SSM). They use a previously trained, constrained model-based algorithm that can account for the deformation of the shape of a structure. Among the SSM, the Active Shape Models (ASM), proposed by Cootes in 1995[16], is one of the most successful. It has been applied to numerous medical imaging applications[17], mainly to construct automatic segmentation frameworks [18–20] by using both intensity and shape variation information. Here, Rüegsegger et al. proposed a semi-automated

method, requiring minimal user interaction to segment the sclera, the cornea and the lens on CT images of adult patients[11].

With the aim of providing an accurate method for eye segmentations in MR images, we present an eye model that can capture both the shape variation and the intensity information from a set of gadolinium enhanced T1-weighted Gradient Echo (GE) VIBE MR sequences used for retinoblastoma imaging. The proposed 3D MRI ASM is, to the best of our knowledge, the first statistical model of the eye based on the MRI data. Importantly, it also involves a fully automatic segmentation of the sclera, the cornea, the lens and the VH. We evaluated our model on a sample of 24 images of healthy children's eyes and validated it quantitatively using a leave-one-out cross validation test. Our experiments show an average DSC of 91.6±2.20% for the ROIs. In addition, we applied our method on two pathological patient eyes with retinoblastoma and have quantitatively highlighted the benefits of our approach with an average DSC of 93.45±0.93%.

Methods and materials

Our segmentation procedure can be summarized as follows. We start by constructing an atlas[21] of the eye regions. We then extract an eye Point-Based Shape Variation Model (PBSVM) and couple it with the intensity information to build an ASM. Then, to segment a new subject, we follow a two steps process. First, we automatically find a number of landmarks within the eye to initialize the alignment of the model, and second, we fit the ASM to the volume. A visual depiction of our framework can be seen in Figure 1.

Training data set and manual segmentation: The dataset used to develop our statistical model is composed of 24 healthy eyes gathered from children aged 3.29±2.15 years (see Figure 2, from 4m to 8y8m). All patient information in our study was anonymized and de-identified by physicians prior to our analysis and the corresponding institution approved the study. MR imaging was performed using a 3T Siemens Verio (Siemens, Erlangen, Germany), with a 32-channel surface head coil attached. The images are gadolinium enhanced T1-weighted GE VIBE[22] (TR/TE, 20/3.91 ms, flip angle, 12 deg) and were acquired with two differing spatial resolutions: 0,416x0.416x0.399 mm and 0.480x0.480x0.499 mm. The images include the head of the patient, both eyes and the optic nerves. Images are resampled to a common voxel spacing of 0.416x0.416x0.399 mm. During imaging, the patients were under general anesthesia[3].

In order to validate our method, an expert radiologist manually segmented all volumes by labeling the following anatomical structures: sclera, cornea, lens, VH and optic disc. As described below, an atlas is then created based on the segmented volumes of every patient. Furthermore, axial length, lens size and width statistics were extracted and compared with the age of the patients. We observed a strong correlation between age and axial length (Figure 2b), as described in Fledelius et al.[23], but a weak correlation between age and lens size and between age and width (Figure 2c-d).

For initialization and detection of the eyes, we apply the method proposed by De Zanet et al.[24], based on the Fast Radial Symmetry (FRST) algorithm. We automatically detect the center of both eyes in all patients (Figure 3a), even in the case of enucleation or pathology. From the dicom file orientation information, we define whether it is the left or right eye. This information enables us to flip the volume over the transversal plane and mirror it for both eyes when required. We then crop the MRI head volume into two smaller Volumes of Interest (VOIs) of size 40x40x40 mm for both eyes. Next, we retrieve the location of the center of the lens, the optic disc, and the VH[24] (Figure 3b). These 3 points provide the initial alignment for building the atlas and for the fitting of a new patient.

Atlas construction: We apply a rigid (*i.e.* translation and rotation) pre-registration step to the whole patient dataset. Both the center of the VH and the lens were used for the translation, and the optic disc position was used for the rotation. We then compute the distance map of the manually

segmented regions, fuse them, and create a baseline atlas. Afterwards, we obtain, for each patient, the deformation field (non-rigid free diffeomorphic demons[25]) against the baseline atlas. Finally, we apply the mean deformation field to the baseline atlas to obtain the atlas in natural coordinate system (NCS)[21].

Point-based Shape Variation Model (PBSVM): We represent the surface of the atlas in NCS as a point cloud by using a mesh extraction algorithm[26]. This is followed by a Gaussian smoothing and a decimation to the regions of the sclera, the cornea and the VH by 85% and by 10% for the lens. The information loss during the decimation step never induced an error over 0.01 mm in average for all ROIs.

Once the surface is extracted, we warp the atlas back to the patient using non-rigid diffeomorphic registration[25]. The new atlas landmark positions for each subject are then transformed to a tangent space (Eq. 1) to preserve the linearity of the PBSVM, as expressed by Cootes[16] in

$$(1)\ x_t = \frac{|\bar{x}|^2}{x * \bar{x}} \cdot x,$$

where x is the original surface points vector, $\bar{x}$ is the mean overall surface shape and x_t is the new projection of the surface points in the tangent space. The Principal Component Analysis (PCA)[27] on the projection is done to extract the principal components of the point cloud distribution in space. The combined information is known as the shape variation model, and is stored in the form of

$$(2)\ x \approx \bar{x} + \Phi b,$$

where $\bar{x}$ is the mean shape, represented as a vector of *t* points, $\Phi = (\varphi_1 | \varphi_2 | \ldots | \varphi_t)$ is a matrix which contains the eigenvectors corresponding to the variation of the model at each point, b is a t-dimensional vector representing the modes of variation. By modifying the b_i value under the constraints $\pm 3\sqrt{\lambda_i}, i = 1..t$, we constrain the model to be within the range of similar shapes to the training set. For every position in b, λ is the eigenvalue corresponding to the Φ matrix. We assume the shape to be represented as a normal distribution of points along shapes $\pm 3\sigma i$[11,16,21].

Active Shape Model (ASM): We connect the PBSVM described in the previous section with the MRI intensity information and create an ASM. In contrast to CT, MRI does not provide fix intensity values across patients. Therefore, we use the standardization equalization algorithm proposed by Nyul et al.[28] to standardize the dataset.

Once the dataset has been equalized, we pre-process the MRI volumes with an anisotropic diffusion gradient filter, and window the image intensity to highlight the region of the eyeball and lens. We fix an arbitrary common upper and lower threshold for the windowing and extract the intensity information at each landmark position. Then, we compute the gradient and the Sobel operators along the intensity profiles normal to the surface. Subsequently, we compute the gradient for the sclera/VH and the Sobel for the lens.

We then select an even distribution of points[29] over the surface of the different regions from the landmark point cloud list (350 points from the sclera-cornea and the VH, and 300 points for the lens). We extract the surface normal at these given points and compute the mean gradient intensities or the mean Sobel profiles, as well as the covariance matrices. The length of the extracted profiles depends on the region. We extract a normalized profile gradient along 11 pixels for the sclera, the cornea and for the VH, and 9 pixels length Sobel profile for the lens.

Automated segmentation: The segmentation of a new patient is as follows. First, the VOI is pre-processed in the same way as the images were processed during the ASM construction; the VOI is not resampled and maintains its original image resolution. We then scan the profiles normal to the surface of the model. These profiles are compared to the intensity profiles provided by the ASM, and a new matched point is set for each profile along the sampled voxels. The fitting is then reduced to an optimization problem where the Mahalanobis distance to the model shape is minimized[16] by reducing the overall distance between the current shape point and the matched point, while constraining the model to be within the deformation range of the PBSVM. In contrast to other works[11], the segmentation scheme that we apply here is twofold: we first fit the sclera and the VH and then once the optimum is found, we fit the lens independently (Figure 3c).

Results

We assessed our segmentation method using a leave-one-out cross-validation test of the ASM. That is, we iterated over each patient, excluding it from the ASM construction and automatically fit the generated model to the excluded patient. The quality of the segmentations were evaluated by computing the Dice Similarity Coefficient (DSC), where we considered the manual segmentation as the ground truth:

$$(3)\ DSC = 2 \cdot \frac{|A \cap B|}{|A|+|B|}$$

Furthermore, for each patient and eye region, we computed the mean distance error between the patient ground truth surface and the automatic segmentation result (Figure 4b). We report the distribution of mean distance error per point across all patients and regions in Figure 5.

The average DSC over all subjects was 94.90±2.12% for the sclera and the cornea, 94.72±1.89% for the VH and 85.16±4.91% for the lens. Figure 4a summarizes the mean DSC. The mean distance error is 0.33±0.17% mm for the sclera and cornea, 0.30±0.15% mm for the VH and 0.17±0.07% mm. for the lens (Figure 4b), with a mean global distribution error of 0.27±0.09 mm per patient. The entire segmentation process takes 14s per eye on average using a Pentium i7 3,4 GHz QuadCore 8GB RAM.

Finally, we applied our segmentation on two patients with retinoblastoma. In these cases, the model was robust in detecting the presence of tumors, even when these were large (Figure 6). We obtained a DSC overlap of 94%, 93.98%, and 92.37% on average for sclera+cornea, VH and lens, respectively.

Discussion

The present work describes a method for automatic segmentation of MRI of the eyes based on 3D ASM. Our approach is, to the best of our knowledge, the first framework for automatic extraction of the eye shape with dedicated regions of the sclera, the cornea, the VH and the lens in the MRI.

We have demonstrated that our model enables to accurately segment the eye, with an average error for all ROIs always under the minimum resolution threshold (0.399 mm) and never reaching more than 1.2mm (Table 1). The results highlight an accurate fit for the posterior part of the VH, where the macula and the optic disc are located (Figure 5a). Furthermore, we noticed a bias towards having over segmentation errors in the frontal part of the eye (Figure 5b-c). This situation caused the lens to yield a lower average DSC (85.16%) than for other regions. The results can be explained due to the

small size of the lens in contrast to the sclera and the VH. This limitation of the DSC index for small regions was already reported by several authors on the field[30,31].

Within the dataset, we identified an outlier (Table 1, Sub07) that presented the lowest accuracy during segmentation across all ROIs. This is due to the small size of the eye (youngest patient with 4 months) that made him not well represented in by our model. In the future, a larger dataset with greater number of younger patients (<6 months) would address this issue. Furthermore, we also observed that Sub03, Sub14 and Sub15 perform below average during the lens fitting. Nevertheless, there is a general trend towards robust segmentation of the sclera, cornea and vitreous humor, even in cases with a strong variation in eye axial length size. The final outcome is that lenses in eyes whose size are closer to the mean shape size are better segmented than extreme-size eyes (Table 2).

Our work demonstrates a novel application of statistical modeling techniques to treatment planning and diagnosis confirmation of intraocular tumors, such as retinoblastoma. The speed, robustness and reliability of the present method are evidence that it can accommodate the variability existing in the size of eyes[23], as well as solving minor eye orientation issues during the fitting process. Similarly to the presented children eye model and pathological eyes, our framework can be directly applied to create a model for adults, for instance, for delineation of the uveal melanoma prior to therapy planning. Uveal melanoma presents a very similar MRI imaging conditions to retinoblastoma, therefore, leveraging the current framework to pathological adult eyes could be the next step.

While previous works attempted to delineate or characterize the MRI imaged eyes using a manual qualitative evaluation[15], we are first to report quantitative results on the segmentation accuracy on MRI. The procedures that we used can provide the basis for objective assessment of the quality of the model fitting in the eye MRI, as it did in other image modalities such as CT[11]. Furthermore, the robustness of the model during the segmentation of pathological MRI volumes indicates an important and promising step towards facilitated treatment planning and tumor extent follow-up. A higher MRI diagnostic accuracy for retinoblastoma, in particular for detection of prelaminar optic nerve and choroidal invasion, is crucial for designing effective treatment strategies. Thus our future work will focus on quantitative evaluation in larger datasets.

To our knowledge, this framework is the most accurate and robust tool yet to fully and automatically segment the lens, sclera, cornea and VH regions in MRI. The presented approach provides a solution for reducing the time spent in delineating the eye shape and is likely to advance current ocular tumor treatment planning and diagnosis techniques.

Figure Legends:

Figure 1: Block diagram representing the fully automatic segmentation framework. We create a model with N-1 Patients and test the performance *on the remaining subject.*

Figure 2: Patient dataset Information. a) Dataset information distribution. b) Age vs. Axial length. c) Age vs. Lens size. d) Age vs. Lens width. Highlighted values in red are Sub03, Sub07, Sub14 and Sub15.

Figure 3: a) MRI volume, highlighting automatic cropping region and landmark initialization. b) Pre-processed MRI region of the eye including landmarks. c) Segmentation results for the lens and the VH.

Figure 4: Leave-one-out cross validation. a) Mean and standard deviation of DSC for independent and combined shapes. b) Mean distance error for every eye region and combined mean error.

Figure 5: Mean distance error distribution with respect to the manual segmentation. a) Unsigned and b-c) signed distance error to display bias towards over-segmentation or under-segmentation.

Figure 6: Patients with retinoblastoma in a) and e). Automatic eye segmentation of a small tumor present in the retina b), c), d). Robust fit of the VH and the Lens for large tumor in f), g), h).

References:

1. Devesa SS. The Incidence of Retinoblastoma. *Am J Ophthalmol*. 1975;80(2):263-265. doi:10.1016/0002-9394(75)90143-9.

2. Balmer a, Zografos L, Munier F. Diagnosis and current management of retinoblastoma. *Oncogene*. 2006;25(38):5341-9. doi:10.1038/sj.onc.1209622.

3. De Graaf P, Göricke S, Rodjan F, et al. Guidelines for imaging retinoblastoma: imaging principles and MRI standardization. *Pediatr Radiol*. 2012;42(1):2-14. doi:10.1007/s00247-011-2201-5.

4. Munier FL, Verwey J, Pica A, et al. New developments in external beam radiotherapy for retinoblastoma: from lens to normal tissue-sparing techniques. *Clin Experiment Ophthalmol*. 2008;36(1):78-89. doi:10.1111/j.1442-9071.2007.01602.x.

5. De Jong MC, de Graaf P, Noij DP, et al. Diagnostic performance of magnetic resonance imaging and computed tomography for advanced retinoblastoma: a systematic review and meta-analysis. *Ophthalmology*. 2014;121(5):1109-18. doi:10.1016/j.ophtha.2013.11.021.

6. Graaf P De, Barkhof F, Moll AC, et al. Retinoblastoma□: MR Imaging Parameters in Detection of Tumor Extent. *Radiology*. 2005;(6):197-207.

7. Fanea L, Fagan AJ. Review: magnetic resonance imaging techniques in ophthalmology. *Mol Vis*. 2012;18(November 2011):2538-60. Available at: http://www.pubmedcentral.nih.gov/articlerender.fcgi?artid=3482169&tool=pmcentrez&rendertype=abstract.

8. Cuadra MB, Gorthi S, Karahanoglu FI, Paquier B, Pica A. Model-based Segmentation and Fusion of 3D Computed Tomography and 3D Ultrasound of the Eye for Radiotherapy Planning. *Second ECCOMAS Themat Conf Comput Vis Med Image Process*. 2009:53-58.

9. Galluzzi P, Hadjistilianou T, Cerase a, De Francesco S, Toti P, Venturi C. Is CT still useful in the study protocol of retinoblastoma? *AJNR Am J Neuroradiol*. 2009;30(9):1760-5. doi:10.3174/ajnr.A1716.

10. Cuadra MB, Gorthi S, Karahanoglu FI, Paquier B, Pica a. Model-based Segmentation and Fusion of 3D Computed Tomography and 3D Ultrasound of the Eye for Radiotherapy Planning. *Second ECCOMAS Themat Conf Comput Vis Med Image Process*. 2009;d:53-58.

11. Rüegsegger MB, Bach Cuadra M, Pica A, et al. Statistical modeling of the eye for multimodal treatment planning for external beam radiation therapy of intraocular tumors. *Int J Radiat Oncol Biol Phys*. 2012;84(4):e541-7. doi:10.1016/j.ijrobp.2012.05.040.

12. Beenakker J-WM, Shamonin DP, Webb a. G, Luyten GPM, Stoel BC. Automated Retinal Topographic Maps Measured With Magnetic Resonance Imaging. *Invest Ophthalmol Vis Sci*. 2015;56:1033-1039. doi:10.1167/iovs.14-15161.

13. Goitein M, Miller T. Planning proton therapy of the eye. *Med Phys*. 10(3):275-83. Available at: http://www.ncbi.nlm.nih.gov/pubmed/6308407.

14. Dobler B, Bendl R. Precise modelling of the eye for proton therapy of intra-ocular tumours. *Phys Med Biol*. 2002;47(4):593-613. doi:10.1088/0031-9155/47/4/304.

15. Singh KD, Logan NS, Gilmartin B. Three-dimensional modeling of the human eye based on magnetic resonance imaging. *Invest Ophthalmol Vis Sci*. 2006;47(6):2272-9. doi:10.1167/iovs.05-0856.

16. Cootes TF, Taylor CJ, Cooper DH, Graham J. Active Shape Models - Their Training and Application. *Comput Vis Image Underst*. 1995;61(1):38-59.

17. Heimann T, Meinzer H-P. Statistical shape models for 3D medical image segmentation: a review. *Med Image Anal*. 2009;13(4):543-63. doi:10.1016/j.media.2009.05.004.

18. Lindner C, Thiagarajah S, Wilkinson JM, Wallis G a, Cootes TF. Fully automatic segmentation of the proximal femur using random forest regression voting. *IEEE Trans Med Imaging*. 2013;32(8):1462-72. doi:10.1109/TMI.2013.2258030.

19. Fritscher KD, Peroni M, Zaffino P, Spadea MF, Schubert R, Sharp G. Automatic segmentation of head and neck CT images for radiotherapy treatment planning using multiple atlases , statistical appearance models , and geodesic active contours Automatic segmentation of head and neck CT images for radiotherapy treatment planni. *Med Phys*. 2014;051910(41). doi:10.1118/1.4871623.

20. Maan B, Heijden F Van Der. Prostate MR image segmentation using 3D Active Appearance Models.

21. Frangi AF, Rueckert D, Schnabel J a, Niessen WJ. Automatic construction of multiple-object three-dimensional statistical shape models: application to cardiac modeling. *IEEE Trans Med Imaging*. 2002;21(9):1151-66. doi:10.1109/TMI.2002.804426.

22. Wetzel SG, Johnson G, Tan AGS, et al. Imaging of the Brain with a Volumetric Interpolated Examination. *AJNR Am J Neuroradiol*. 2002;23(July):995-1002.

23. Fledelius HC, Christensen a C. Reappraisal of the human ocular growth curve in fetal life, infancy, and early childhood. *Br J Ophthalmol*. 1996;80(10):918-21. Available at: http://www.pubmedcentral.nih.gov/articlerender.fcgi?artid=505651&tool=pmcentrez&rendertype=abstract.

24. De Zanet SI, Ciller C, Rudolph T, et al. Landmark detection for fusion of fundus and MRI toward a patient-specific multimodal eye model. *IEEE Trans Biomed Eng*. 2015;62(2):532-40. doi:10.1109/TBME.2014.2359676.

25. Vercauteren T, Pennec X, Perchant A, Ayache N. Diffeomorphic demons: efficient non-parametric image registration. *Neuroimage*. 2009;45(1 Suppl):S61-72. doi:10.1016/j.neuroimage.2008.10.040.

26. Lorensen WE, Cline HE. Marching cubes: A high resolution 3D surface construction algorithm. *ACM SIGGRAPH Comput Graph*. 1987;21(4):163-169. doi:10.1145/37402.37422.

27. Jolliffe IT, Edition S. Principal Component Analysis. 2008.

28. Nyúl LG, Udupa JK. On standardizing the MR image intensity scale. *Magn Reson Med*. 1999;42(6):1072-81. Available at: http://www.ncbi.nlm.nih.gov/pubmed/10571928.

29. Vogel H. A better way to construct the sunflower head. *Math Biosci*. 1979;44(3-4):179-189. doi:10.1016/0025-5564(79)90080-4.

30. Peroni M, Spadea MF, Riboldi M, et al. Validation of Automatic Contour Propagation for 4D Treatment Planning using Multiple Metrics. *Technol Carcer Res Treat*. 2013;12(6):501-510. doi:10.7785/tcrt.2012.500347.

31. Rohlfing T. Image similarity and tissue overlaps as surrogates for image registration accuracy: Widely used but unreliable. *IEEE Trans Med Imaging*. 2012;31(2):153-163. doi:10.1109/TMI.2011.2163944.

Figure 1

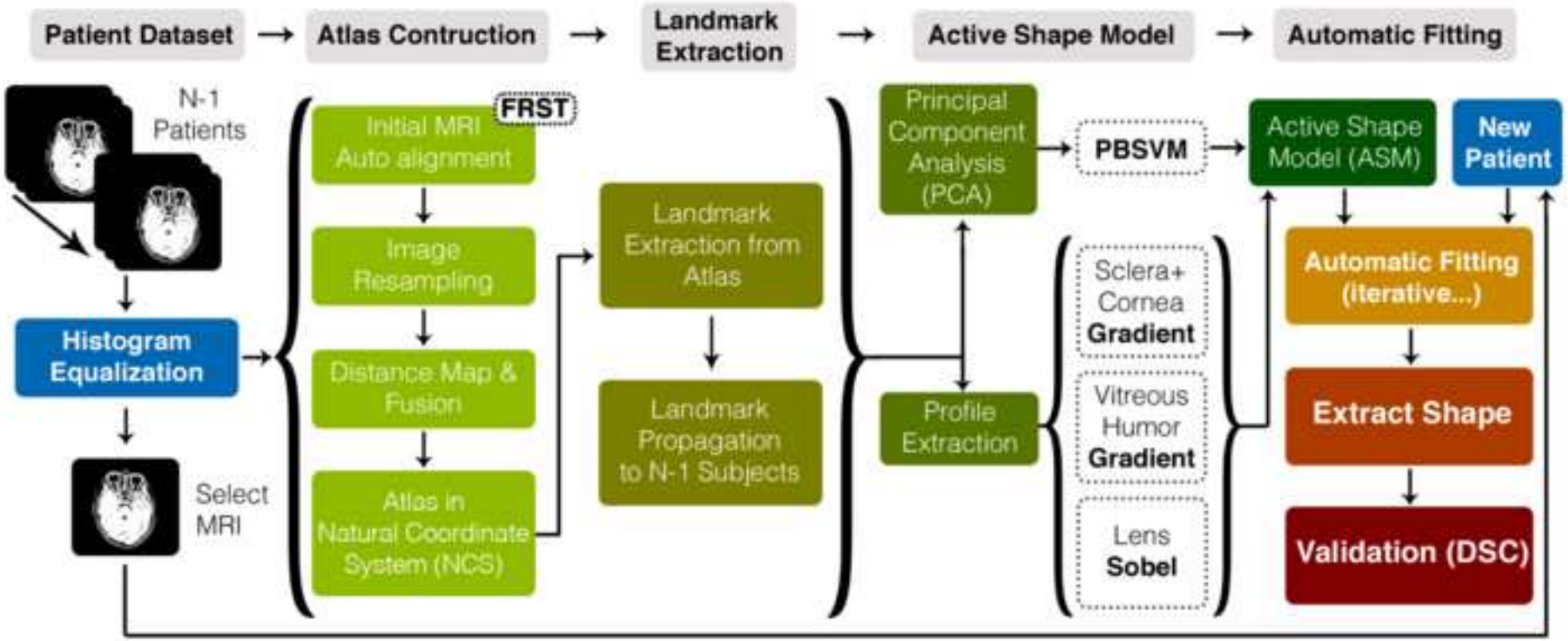
Patient Dataset
Atlas Contruction
Landmark Extraction
Active Shape Model
Automatic Fitting
N-1 Patients
Histogram Equalization
Select MRI
FRST
Initial MRI Auto alignment
Image Resampling
Distance Map & Fusion
Atlas in Natural Coordinate System (NCS)
Landmark Extraction from Atlas
Landmark Propagation to N-1 Subjects
Principal Component Analysis (PCA)
Profile Extraction
PBSVM
Sclera+ Cornea Gradient
Vitreous Humor Gradient
Lens Sobel
Active Shape Model (ASM)
New Patient
Automatic Fitting (iterative...)
Extract Shape
Validation (DSC)

Figure 2

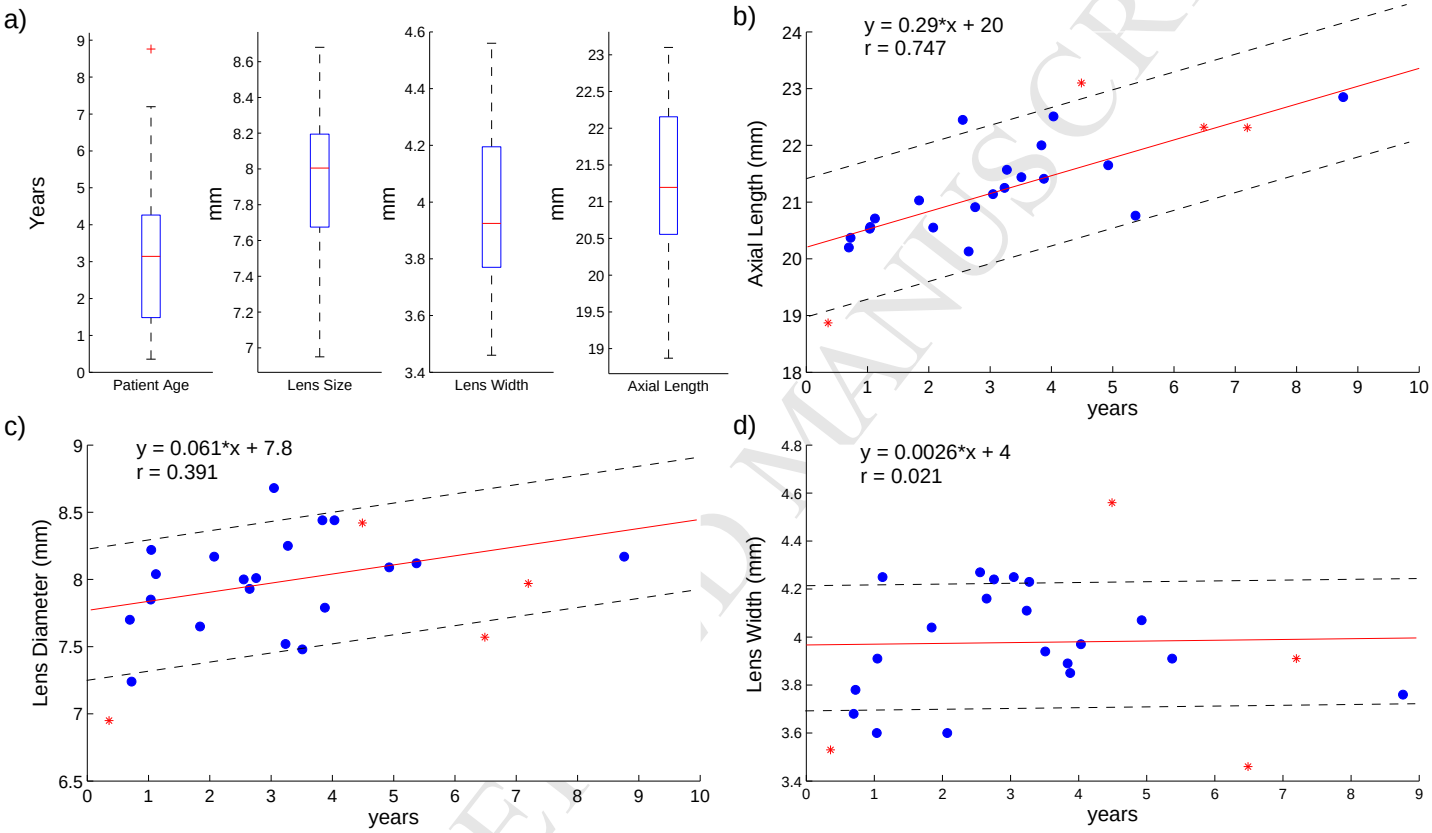

Figure 3

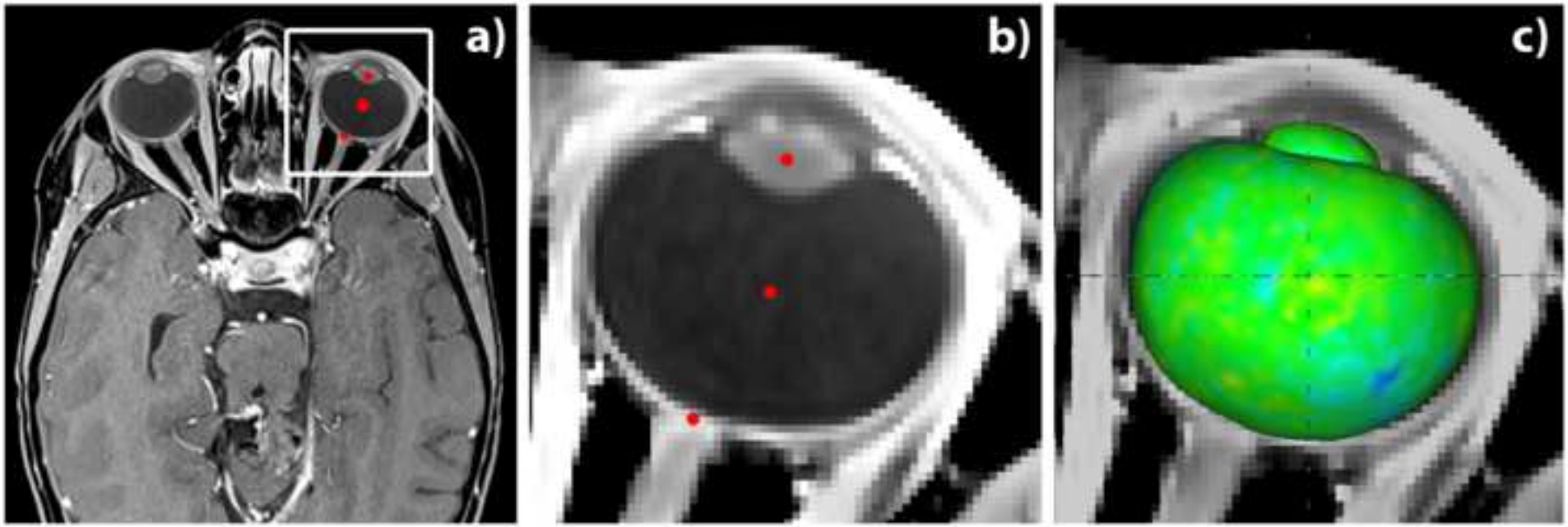

Figure 4

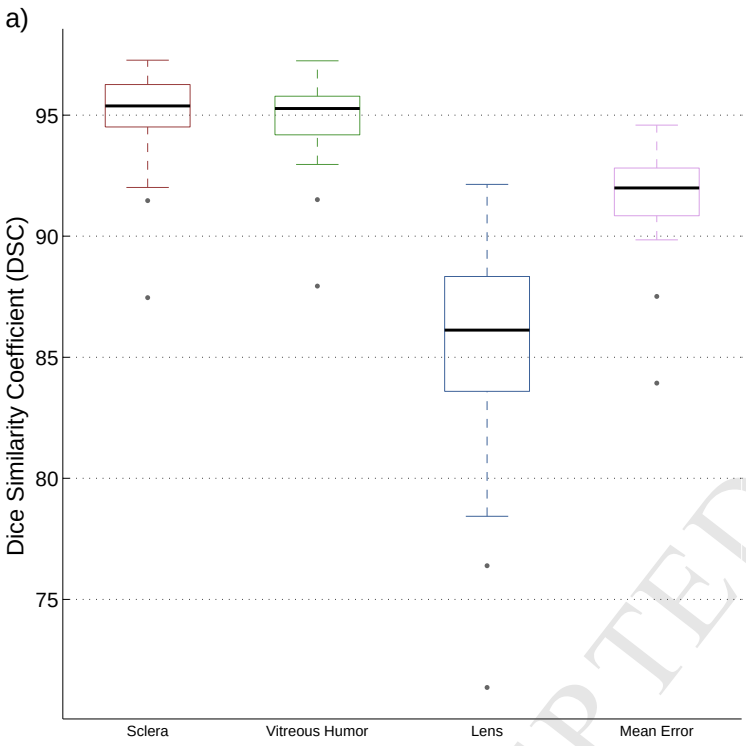

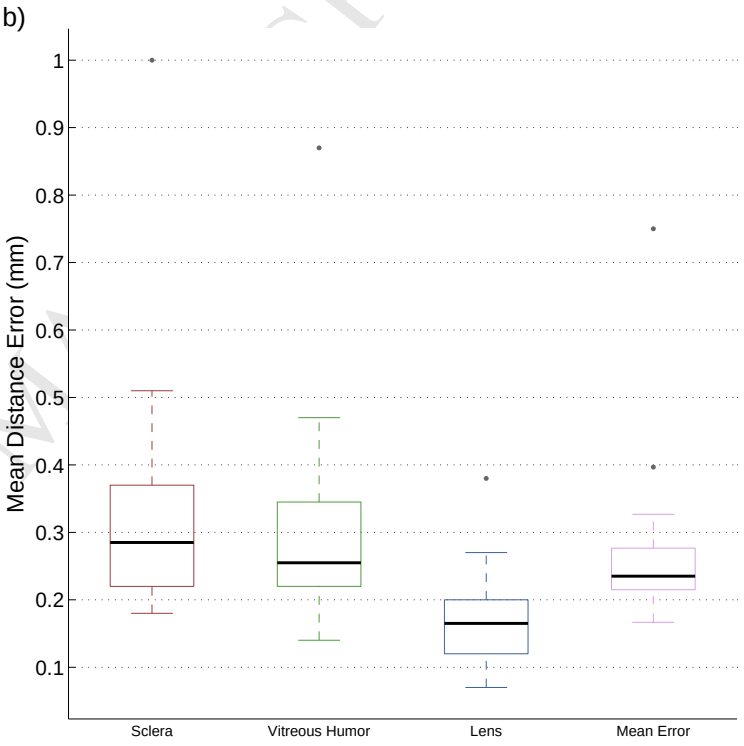

Figure 5

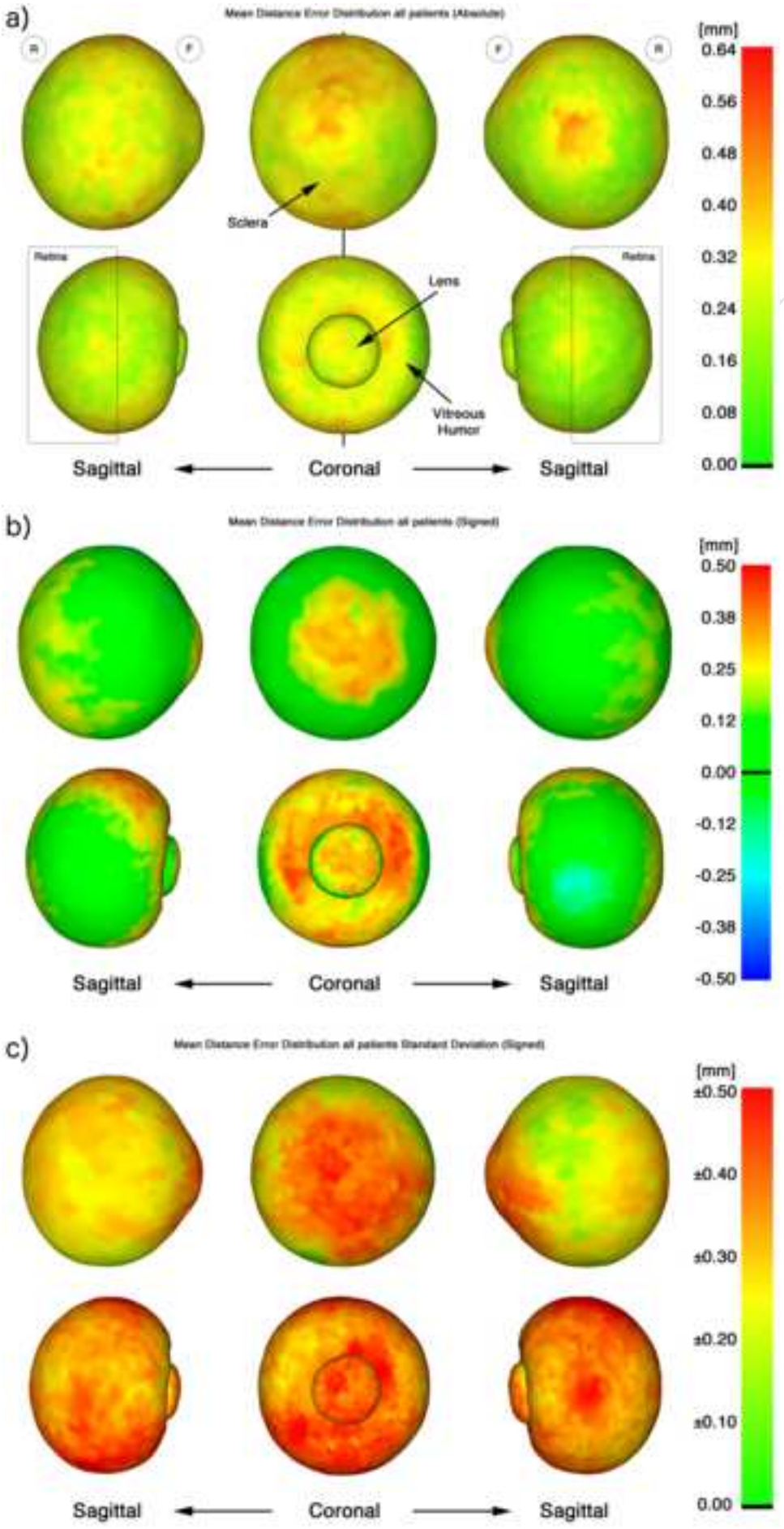
a)
Mean Distance Error Distribution all patients (Absolute)
[mm]
0.64
0.56
0.48
0.40
0.32
0.24
0.16
0.08
0.00
Sclera
Lens
Vitreous Humor
Retina
Retina
Sagittal
Coronal
Sagittal
b)
Mean Distance Error Distribution all patients (Signed)
[mm]
0.50
0.38
0.25
0.12
0.00
-0.12
-0.25
-0.38
-0.50
Sagittal
Coronal
Sagittal
c)
Mean Distance Error Distribution all patients Standard Deviation (Signed)
[mm]
±0.50
±0.40
±0.30
±0.20
±0.10
0.00
Sagittal
Coronal
Sagittal

Figure 6

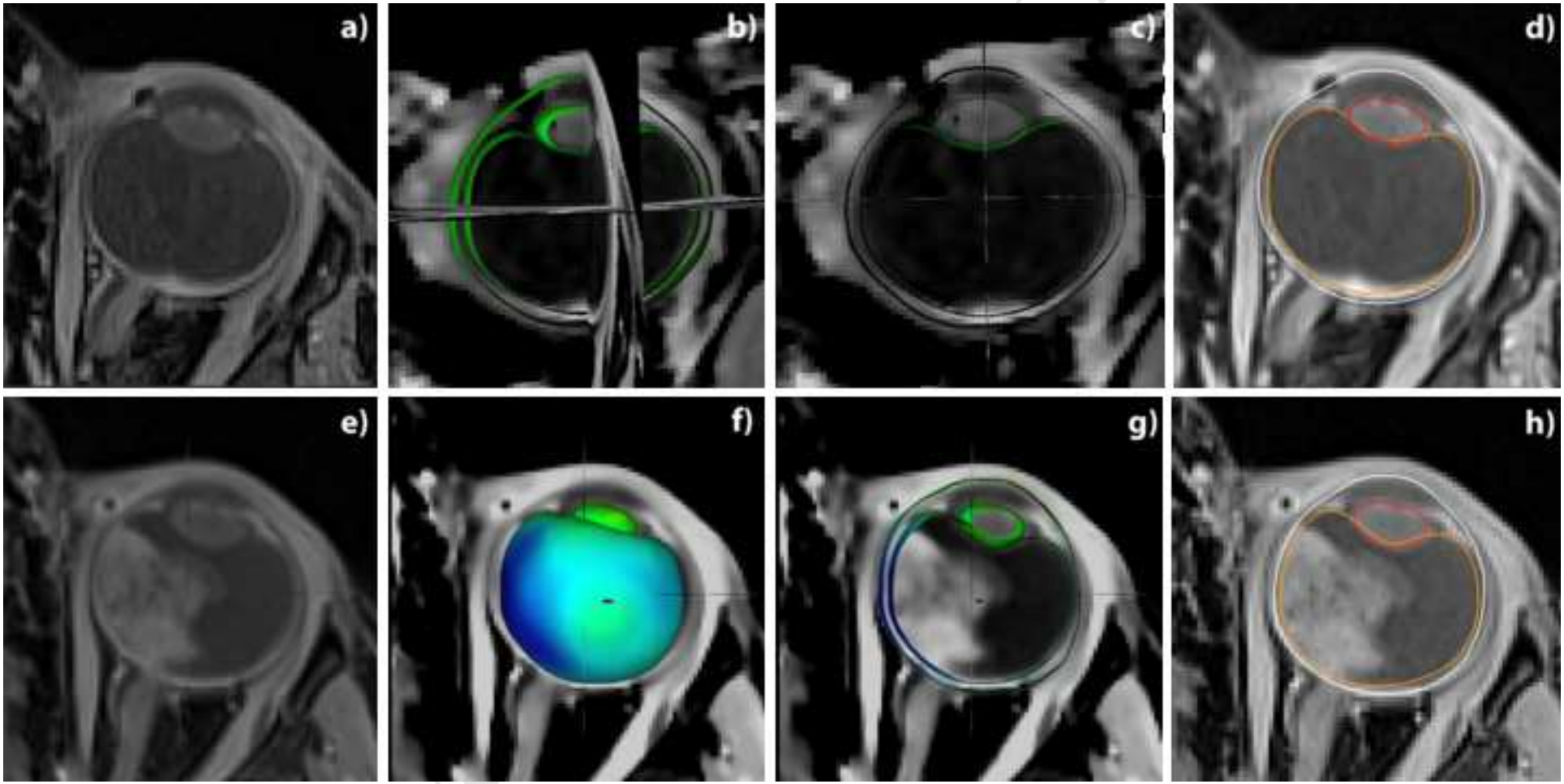

Table 1: Dice Similarity Coefficient (DSC) for Active Shape Model during leave-one-out cross-validation test. Mean overall error in (mm).

	Sclera	V.H.	Lens	Mean DSC	Sclera	Scl. Dev.	Max. Sclera	VH	VH Dev.	Max. VH	Lens	Lens Dev.	Max. Lens
Sub01	96.23	95.60	86.75	92.93	0.36	0.07	1.19	0.39	0.08	1.19	0.10	0.03	0.57
Sub02	92.01	94.51	84.15	90.16	0.33	0.1	0.79	0.25	0.06	1.15	0.14	0.04	0.59
Sub03	94.89	94.80	79.85	89.34	0.28	0.09	1.59	0.23	0.06	0.99	0.16	0.04	0.57
Sub04	95.94	95.39	86.70	92.73	0.39	0.11	1.59	0.19	0.06	1.15	0.15	0.04	0.57
Sub05	96.51	95.94	81.79	91.57	0.29	0.06	0.93	0.34	0.08	1.24	0.08	0.03	0.57
Sub06	93.62	95.49	92.14	93.35	0.19	0.06	0.57	0.14	0.04	0.83	0.19	0.04	0.58
Sub07	87.46	87.94	76.39	84.20	1	0.22	2.38	0.87	0.19	2.46	0.38	0.1	1.25
Sub08	94.36	95.22	87.09	92.14	0.21	0.05	0.83	0.17	0.04	0.83	0.27	0.06	0.83
Sub09	97.27	96.69	87.46	93.37	0.25	0.05	0.9	0.3	0.06	1.19	0.07	0.02	0.41
Sub10	95.03	94.05	89.21	92.80	0.35	0.12	1.52	0.43	0.13	1.51	0.12	0.04	0.59
Sub11	96.45	97.24	90.07	94.40	0.45	0.07	1.27	0.22	0.06	0.9	0.11	0.03	0.57
Sub12	95.27	95.32	90.07	93.76	0.25	0.07	0.9	0.28	0.08	1.25	0.17	0.04	0.59
Sub13	94.66	93.67	85.60	91.35	0.38	0.16	2.03	0.43	0.17	2.04	0.17	0.04	0.83
Sub14	96.29	95.95	78.43	90.50	0.18	0.06	1.15	0.25	0.09	1.46	0.21	0.05	0.57
Sub15	96.17	95.01	71.36	87.69	0.19	0.05	0.79	0.26	0.08	1.71	0.25	0.07	0.93
Sub16	91.47	93.67	86.25	90.78	0.34	0.1	0.58	0.23	0.06	0.9	0.17	0.04	0.71
Sub17	96.54	95.13	83.60	91.70	0.19	0.05	0.92	0.15	0.04	0.83	0.23	0.07	0.93
Sub18	95.46	94.32	87.11	92.41	0.23	0.05	0.93	0.2	0.05	0.83	0.14	0.04	0.57
Sub19	93.80	91.51	91.52	92.34	0.23	0.06	0.83	0.26	0.06	0.58	0.17	0.04	0.59
Sub20	96.80	95.79	89.63	94.15	0.34	0.08	1.25	0.3	0.06	0.93	0.17	0.04	0.59
Sub21	95.71	95.77	83.58	91.60	0.2	0.06	1.19	0.22	0.08	1.27	0.08	0.03	0.42
Sub22	95.30	92.96	85.40	91.14	0.27	0.07	1.15	0.25	0.08	0.79	0.16	0.04	0.83
Sub23	94.82	95.89	85.99	92.44	0.5	0.09	1.31	0.35	0.07	1.24	0.12	0.04	0.58
Sub24	95.50	95.43	83.72	91.66	0.51	0.04	0.99	0.47	0.04	0.93	0.21	0.07	0.93
Mean	94.90	94.72	85.16	91.60	0.33	0.08	1.15	0.30	0.08	1.18	0.17	0.04	0.67
SD	2.12	1.89	4.91	2.20	0.17	0.04	0.43	0.15	0.04	0.43	0.07	0.17	0.19

Table 2: Patient Dataset Information – Age, lens size, lens width and axial length

	Age (y.)	Lens Size (mm)	Lens Width (mm)	Axial Length (mm)
Sub01	3.510	7.48	3.94	21.44
Sub02	3.877	7.79	3.85	21.41
Sub03	6.488	7.57	3.46	22.32
Sub04	3.838	8.44	3.89	22
Sub05	0.696	7.7	3.68	20.2
Sub06	4.926	8.09	4.07	21.65
Sub07	0.356	6.95	3.53	18.87
Sub08	4.033	8.44	3.97	22.51
Sub09	5.373	8.12	3.91	20.76
Sub10	1.036	7.85	3.6	20.53
Sub11	2.071	8.17	3.6	20.55
Sub12	2.756	8.01	4.24	20.91
Sub13	2.649	7.93	4.16	20.13
Sub14	7.197	7.97	3.91	22.31
Sub15	4.490	8.42	4.56	23.1
Sub16	8.762	8.17	3.76	22.85
Sub17	3.236	7.52	4.11	21.25
Sub18	2.553	8	4.27	22.45
Sub19	3.274	8.25	4.23	21.57
Sub20	1.044	8.22	3.91	20.56
Sub21	1.841	7.65	4.04	21.03
Sub22	3.047	8.68	4.25	21.14
Sub23	1.121	8.04	4.25	20.71
Sub24	0.723	7.24	3.78	20.37
Mean	3.29	7.94	3.97	21.27
SD	2.15	0.40	0.27	1.00

SIEMENS MAGNETOM Verio syngo MR B17

TA: 6:19 PAT: Voxel size: 0.4×0.4×0.4 mm Rel. SNR: 1.00 SIEMENS: fl3d_vibe

Properties	
Prio Recon	Off
Before measurement	
After measurement	
Load to viewer	On
Inline movie	Off
Auto store images	On
Load to stamp segments	Off
Load images to graphic segments	Off
Auto open inline display	Off
Start measurement without further preparation	On
Wait for user to start	Off
Start measurements	single

Routine	
Slab group 1	
Slabs	1
Dist. factor	20 %
Position	R5.2 P17.4 F3.9
Orientation	T > S-2.6 > C-0.7
Phase enc. dir.	R >> L
Rotation	94.80 deg
Phase oversampling	0 %
Slice oversampling	38.5 %
Slices per slab	104
FoV read	200 mm
FoV phase	100.0 %
Slice thickness	0.40 mm
TR	20.0 ms
TE	3.89 ms
Averages	1
Concatenations	1
Filter	Distortion Corr.(2D), Prescan Normalize, Elliptical filter
Coil elements	HEA;HEP

Contrast	
Flip angle	12.0 deg
Fat suppr.	Q-fat sat.
Lines Per Shot	72
Water suppr.	None
Dixon	No Dixon
Save original images	On
Averaging mode	Short term
Reconstruction	Magnitude
Measurements	1
Multiple series	Each measurement

Resolution	
Base resolution	480
Phase resolution	100 %
Slice resolution	63 %
Phase partial Fourier	Off
Slice partial Fourier	6/8
Interpolation	Off
PAT mode	GRAPPA
Accel. factor PE	2
Ref. lines PE	24
Accel. factor 3D	1
Matrix Coil Mode	Auto (Triple)
Reference scan mode	Integrated
Image Filter	Off
Distortion Corr.	On
Mode	2D
Unfiltered images	Off
Unfiltered images	Off
Prescan Normalize	On
Normalize	Off
B1 filter	Off
Raw filter	Off
Elliptical filter	On
Mode	Inplane
POCS	Off

Geometry	
Multi-slice mode	Sequential
Series	Ascending
Special sat.	None
Set-n-Go Protocol	Off
Table position	H
Table position	0 mm
Inline Composing	Off

System	
Body	Off
HEP	On
HEA	On
SP4	Off
SP2	Off
SP8	Off
SP6	Off
SP3	Off
SP1	Off
SP7	Off
SP5	Off
Positioning mode	FIX
MSMA	S - C - T
Sagittal	R >> L
Coronal	A >> P
Transversal	F >> H
Save uncombined	Off
Coil Combine Mode	Adaptive Combine
AutoAlign	—
Auto Coil Select	Default
Shim mode	Standard
Adjust with body coil	On
Confirm freq. adjustment	Off
Assume Silicone	Off
? Ref. amplitude 1H	0.000 V
Adjustment Tolerance	Auto
Adjust volume	
Position	R5.2 P17.4 F3.9
Orientation	T > S-2.6 > C-0.7
Rotation	94.80 deg
A >> P	200 mm
R >> L	200 mm
F >> H	42 mm

Physio	
1st Signal/Mode	None
Resp. control	Off

Inline	
3D centric reordering	Off

SIEMENS MAGNETOM Verio syngo MR B17

Time to center	181.5 s
Subtract	Off
Liver registration	Off
Std-Dev-Sag	Off
Std-Dev-Cor	Off
Std-Dev-Tra	Off
Std-Dev-Time	Off
MIP-Sag	Off
MIP-Cor	Off
MIP-Tra	Off
MIP-Time	Off
Save original images	On
Wash - In	Off
Wash - Out	Off
TTP	Off
PEI	Off
MIP - time	Off
MapIt	None
Contrasts	1

Sequence

Introduction	On
Dimension	3D
Elliptical scanning	Off
Reordering	Centric
Asymmetric echo	Weak
Bandwidth	130 Hz/Px
Optimization	None
Allowed delay	0 s
RF pulse type	Normal
Gradient mode	Fast
Excitation	Slab-sel.
RF spoiling	On

Atlas Construction:

The process to construct the atlas follows the lines of Frangi et al.[1]. However, we introduce minor modifications to the original method, such as a rigid volume pre-alignment based on landmarks in the eye in the MRI[2], and a non-rigid free diffeomorphic demons registration algorithm[3] to transform the atlas into a Natural Coordinate System (NCS)[1].

We first align every MRI volume to a common reference coordinate system. We apply, to each subject, a rigid pre-alignment using the landmarks from De Zanet et al.[2] based on 3D FRST[4]. The center of the vitreous humor, the center of the lens and the position of the optic disc help us to align all patients into a common reference space. Once the complete dataset is aligned, we resample all MRI volumes to 0.416x0.416x0.399 mm. Afterwards, we compute a voxel signed distance map of the different labeled regions and fuse them to create the baseline atlas.

To reduce the bias towards a certain shape, we register the baseline atlas against each manually segmented region using a non-rigid free diffeomorphic demons, and apply the transformation to the baseline atlas. This process enables us to combine all the deformation fields together and transform the current baseline atlas into an unbiased NCS atlas.

Point-Based Shape Variation Model (PBSVM):

Once the atlas in NCS has been built, we extract a surface point cloud for every eye atlas region: sclera + cornea, vitreous humor and lens. To obtain this information, we utilize a mesh extraction algorithm[5]. It is important to highlight that the binary mesh extraction step generally provides us with a non-smoothed point based surface; therefore, to have a proper smoothed point distribution, we require to apply a Gaussian smoothing filter[6]. The number of iterations that we do over each surface is 50, with a band-pass filter of 0.01.

The current point cloud represents a smoothed approximation of the original NCS atlas shape. We apply a decimation to each of the point cloud surfaces[5] and reduce the number of points to a 15% of the original amount for the sclera + cornea and the vitreous humor, and to a 90% of the original amount for the lens. These new set of points will later be used as landmarks to capture the patient variability. An important remark concerning the decimation process is that the algorithm aims at preserving the topology of the surface, therefore, it will preserve important details, such as the point curvature.

Once the surfaces are decimated, we perform a non-rigid free diffeomorphic demons registration between the original volumes and the NCS atlas, and warp the atlas landmark point cloud back to the patients[3]. This process enables us retrieve information about every landmark position in each the patient. The corresponding landmark positions are used to capture the landmark variability, which is later encoded inside the PBSVM through a Principal Component Analysis (PCA)[7]. To perform this process, we start by transforming the point cloud into a tangent space (eq. 1), thus preserving the linearity of the shape (Eq. 1)

$$(1)\ \mathrm{x_t} = \frac{|\bar{\mathrm{x}}|^2}{\mathrm{x} * \bar{\mathrm{x}}} \cdot \mathrm{x},$$

This approach follows the lines of Cootes et al.[8], where x is the original surface points vector, $\bar{\mathrm{x}}$ is the mean surface shape and $\mathrm{x_t}$ is the new projection of the surface points in the tangent space. We then compute the PCA of the projection, and extract the principal components of the landmark point cloud distribution in the space. This extracted information is stored in the form of

(2) $x \approx \bar{x} + \Phi b$,

where $\bar{x}$ is the mean shape, represented as a vector of t points, $\Phi = (\varphi_1|\varphi_2|\ldots|\varphi_t)$ is a matrix which contains the eigenvectors corresponding to the variation of the model at each point and b is a t-dimensional vector representing the modes of variation, and is widely know as point based shape variation model (PBSVM). This PBSVM is normally constrained between the values $\pm 3\sqrt{\lambda_i},\ i = 1..t$, to be within the range of similar shapes to the ones used during the model construction (Fig. 7).

To apply these constraints, we assume that the shapes are represented as a normal distribution of points across subjects. We could arbitrarily relax the region constraints and increase the maximum allowed deformation, however, we opted to limit it and to create a robust model, able to cope with potential pathologies or abnormalities inside the eye.

Active Shape Model:

We combine both the PBSVM and the MRI profile intensity information from the subject dataset to create an ASM. MRI does not provide homogeneous intensity values across subjects and structures; therefore, we require a reliable standardization algorithm to equalize the dataset. The standardization algorithm proposed by Nyul et al.[9] proved to be a simple yet reliable equalization method.

Then, prior to extracting the image profile information, we perform a set of image pre-processing techniques. First, we start by applying a gradient anisotropic diffusion filter[10] on the standardized images, with a conductance parameter of 1 and run 15 iterations. The filter will remove existing MRI noise while preserving important anatomical region edges. Second, we fix an arbitrary lower and upper threshold and filter the image to remove low and high intensity information. The objective is to achieve a good contrast between the anterior chamber and the lens, while preserving a good contrast of the vitreous humor and sclera region. Finally, we compute both the gradient (with a 1 voxel size kernel) and the Sobel operator of the windowed image.

The gradient gives us the profile information for the regions of the sclera + cornea and the vitreous humor. The Sobel operator provides the information about the lens region. Once processed, we retrieve the landmark point cloud information that we extracted in the previous (PBSVM) section and select an even distribution of points[11] over the surface of the different layers. We extract 350 points for the regions of the sclera + cornea and the vitreous humor and 300 points for the region of the lens.

The corresponding landmark point clouds across subjects allow us to extract the profiles normal to the surface and compute the mean profile intensity (for both Gradient and Sobel) and the covariance matrix across profiles.

The length of the profile depends on the region of interest. For the region of the sclera + cornea and the vitreous humor we select a profile length of 11 voxels. For the region of the lens we select a profile length of 9 voxels. An important remark concerning the profile extraction step is that whenever we encounter a profile whose Gradient/Sobel is not strong enough, we do not include it in the model. This profile selection process allows us to actively build the model with the strongest Gradient/Sobel profiles and increase the quality of the fitting during the automatic segmentation stage.

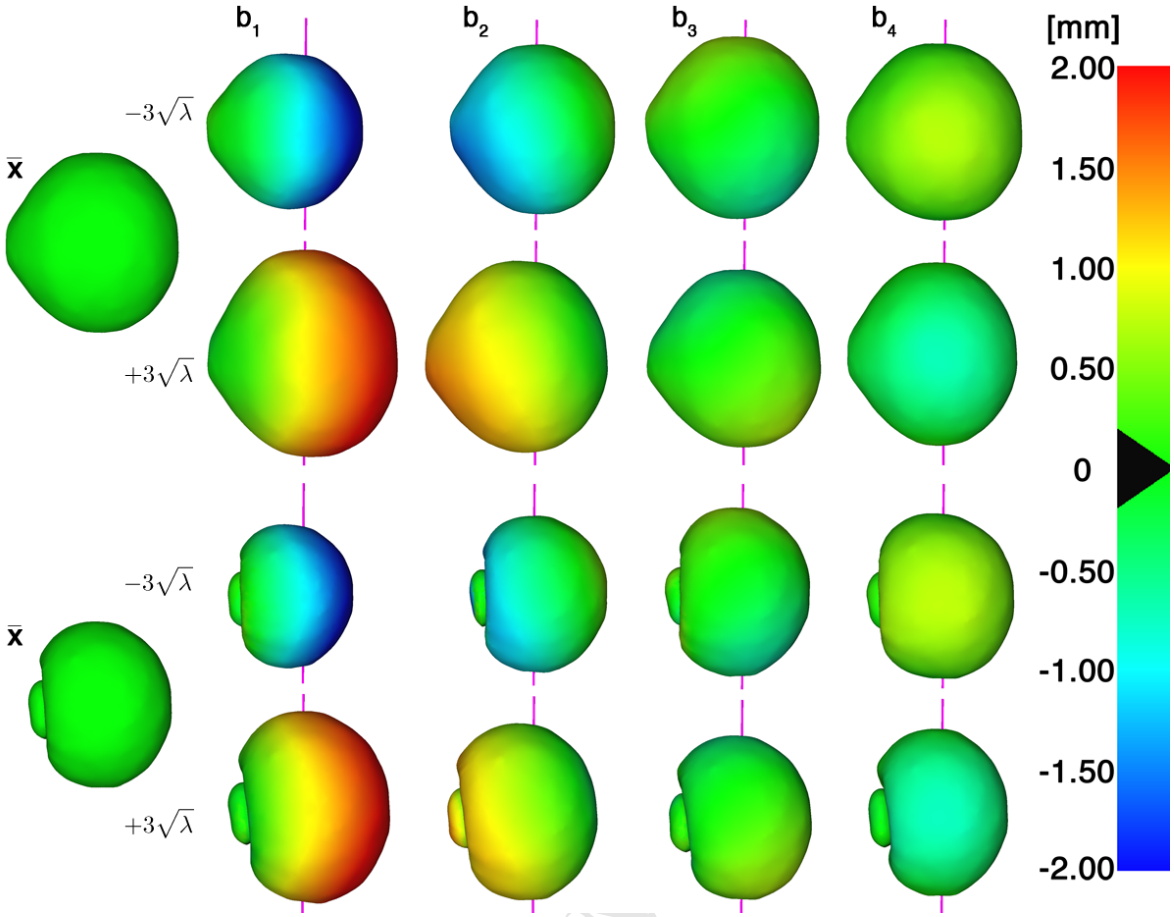

Fig. 7: Model mean shape ($\bar{x}$) indicating the region of the sclera (upper left) and the vitreous humor and the lens (down left). First, second, third and fourth (b_1,b_2,b_3,b_4) mode of variation and effects in shape deformation colored in mm. with respect to the distance to the mean shape.

References:

1. Frangi AF, Rueckert D, Schnabel J a, Niessen WJ. Automatic construction of multiple-object three-dimensional statistical shape models: application to cardiac modeling. *IEEE Trans Med Imaging*. 2002;21(9):1151-66.

2. Zanet SI De, Ciller C, Rudolph T, et al. Landmark Detection for Fusion of Fundus and MRI Towards a Patient-Specific Multi-Modal Eye Model. *IEEE Trans Biomed Eng*. 2014;99(xx):1-9.

3. Vercauteren T, Pennec X, Perchant A, Ayache N. Diffeomorphic demons: efficient non-parametric image registration. *Neuroimage*. 2009;45(1 Suppl):S61-72.

4. Loy G, Zelinsky A. A Fast Radial Symmetry Transform for Detecting Points of Interest. Pattern Analysis and Machine Learning Intelligence, IEEE Transactions on. 2003, 25(8):959-973.

5. Lorensen WE, Cline HE. Marching cubes: A high resolution 3D surface construction algorithm. *ACM SIGGRAPH Comput Graph*. 1987;21(4):163-169.

6. Zhang T, Golub G. Research Report - Optimal Surface Smoothing as Filter Design. 1996;20404.

7. Jolliffe IT, Edition S. Principal Component Analysis. 2008.

8. Cootes TF, Taylor CJ, Cooper DH, Graham J. Active Shape Models - Their Training and Application. *Comput Vis Image Underst*. 1995;61(1):38-59.

9. Nyúl LG, Udupa JK. On standardizing the MR image intensity scale. *Magn Reson Med*. 1999;42(6):1072-81.

10. Perona P, Malik J. Scale-space and edge detection using anisotropic diffusion. *IEEE Trans Pattern Anal Mach Intell*. 1990;12(7):629-639.

11. Vogel H. A better way to construct the sunflower head. *Math Biosci*. 1979;44(3-4):179-189.